ChemElectroChem

Research Article
doi.org/10.1002/celc.202300339

Chemistry Europe
European Chemical Societies Publishing

www.chemelectrochem.org

# Metal Carbide Additives in Graphite-Silicon Composites for Lithium-Ion Batteries

Juan Piñuela-Noval,[a] Daniel Fernández-González,[a] Sergio Brutti,[b] Marta Suárez,[a] Franco Mazzei,[c] Maria Assunta Navarra,[b] Luis Felipe Verdeja,[d] Adolfo Fernández,[a] and Marco Agostini*[c]

The pathway for improving lithium-ion batteries' energy density strongly depends on finding materials with enhanced performance. Although great efforts have been done, on the anode-side, graphite is still the best choice. In the last decade, silicon elements are attracting growing attention as anode since their use can theoretically increase specific capacity of the negative electrode side. However, as the electrochemical mechanism involves the alligation of a large amount of Li, the silicon electrode experiences huge volume changes (more than 300% of its initial volume), leading to fractures and pulverizations of the electrode. Herein, we propose for the first time using Molybdenum and Chromium Carbides as additive to stabilize graphite/silicon composites. Spark plasma sintering technology is used to sinter the electrode powders. We demonstrated that the presence of molybdenum or chromium carbides promotes the performance of C/Si electrodes, improving the cycling stability compared to pristine graphite/silicon electrodes.

## Introduction

Lithium-ion batteries are today widely employed in portable electronic markets as the possibility to get a fast charging rate with good durability. Recently, the need to reduce fossil fuels paved the attention to employing such devices in powering electric vehicles, with the final goal of going zero emission in a short period. However, several reasons hinder the widespread of such technology in electric cars.[1] Among the others is the low energy density limited by using electrodic materials with low specific capacity.[2,3] One of that is the anode side, today commercially constituted by graphite-based electrodes, with Lithium storage thermodynamically limited by the intercalation-deintercalation mechanism of $Li^+$ in graphene layers (372 mAh $g^{-1}$).[1,4–6] As an alternative to graphite anode, silicon attracted growing attention due to its high theoretical capacity (3579 mAh $g^{-1}$) thanks to the alloying chemistry during lithiation ($Li_{15}Si_4$), the low working potential (about 0.4 V vs. $Li^+$/Li), the natural abundance and the non-toxicity.[1] However, the development of commercial silicon anodes is still a big challenge as massive volume changes of silicon particles (more than 300%) during the (de)lithiation process, which leads to fracture of the silicon and deformation of the electrode, pulverization and delamination.[1,7]

Furthermore, Si particles catalyze the decomposition of the electrolyte with the uncontrollable growth of solid electrolyte interface while being semi-conductor with low electronic conductivity of $6.7\times10^{-1}$ S $cm^{-1}$ which limits the rate charge.[7–10] To address the problems above, different approaches have been proposed in the last decade; one of these is to employ nanostructured Si (nanoparticles, yolk-shell, nanowires etc.),[11–13] composites,[14–16] polymer binders,[17–19] and additives[19,20] to improve Si-electrode performance in Li-cells. Involving metal carbides in silicon anodes is an additional strategy not yet explored to increase the capacity and cycle-life. Firstly, composite silicon/wolfram carbide@graphene with a particular microstructure has been reported to maintain high initial coulombic efficiency and long cycle life, alleviating structural changes.[21] In contrast, metal carbides ($Mo_2C$, $Cr_2C_3$, etc.) in the form of Si–$Cr_3C_2$@few-layer graphene and Si–$Mo_2C$@few-layer graphene electrodes were also reported with good electrochemical performance.[22] Furthermore, carbides, in general, can also provide an excellent conductive skeleton to improve the electronic conductivity of Si, thanks to the presence of nano-conductive channels that reduce electron transfer resistance.[23,24]

[a] J. Piñuela-Noval, Dr. D. Fernández-González, Dr. M. Suárez, Dr. A. Fernández
Nanomaterials and Nanotechnology Research Center (CINN-CSIC)
Universidad de Oviedo (UO)
Principado de Asturias (PA), Avda. de la Vega, 4–6, 33940, El Entrego (Spain)

[b] Prof. Dr. S. Brutti, Prof. Dr. M. A. Navarra
Department of Chemistry
"Sapienza" University of Rome
P.le Aldo Moro 5, 00185 Rome (Italy)

[c] Prof. Dr. F. Mazzei, Dr. M. Agostini
Department of Chemistry and Technology of Drugs
"Sapienza" University of Rome
P.le Aldo Moro 5, 00185 Rome (Italy)
E-mail: marco.agostini@uniroma1.it

[d] Prof. Dr. L. F. Verdeja
Departamento de Ciencia de los Materiales e Ingeniería Metalúrgica
Escuela de Minas, Energía y Materiales
Universidad de Oviedo
Calle Independencia, s/n, 33004, Oviedo/Uviéu, Asturias (Spain)

Supporting information for this article is available on the WWW under https://doi.org/10.1002/celc.202300339

This paper reports on using carbides (Mo and Cr based) in graphite-silicon composites for lithium-ion batteries. A simple to scale two-step process, consisting first in the formation of metallic carbides (molybdenum or chromium) in the matrix of graphite using spark plasma sintering technology and then in mixing graphite/carbides with Si nanoparticles (< 250 nm) by ball milling was reported. Electrochemical performance is investigated and compared with standard graphite/Si nanoparticle electrodes. The results demonstrated how the presence of carbides stabilized the electrochemical performance regarding coulombic efficiency and cycling stability.

## Results and discussion

Starting from battery-grade graphitic powder, a first electrodic powder was synthesized by dispersing 20% Si nanoparticles in commercial graphite powder (see experimental section); the obtained material was called GHDR 15–4. A second material was synthesized using graphitic powder named Asbury, following dispersing of 20% Si. The third material was synthesized by including in the graphitic matrix of Asbury 5% MoC and 20% Si nanoparticles, named Asbury-MoC. A fourth material was obtained mixing in the graphite 5% $Cr_3C_2$ and 20% Si nanoparticles, called Asbury-$Cr_3C_2$. All materials were first characterized by the use of X-ray diffraction (XRD), Figure 1a. All samples showed the presence of typical graphite and Si peaks, moreover, with reduced intensity for the sample, MoC (green) and $Cr_3C_2$ (orange) peaks, respectively. Raman spectroscopy was also performed for all samples, Figure 1b; corresponding Raman spectra highlighted peaks related to crystalline silicon (around 520 $cm^{-1}$).[25,26] Furthermore, D- and G-bands (Figure 1c), typical of carbon-based materials, were detected close at 1350 and 1580 cm-1.[26,27] G-band intensity is higher than D-band for all samples because of an ordered graphitic matrix.[25] Intensity ratio between D and G peaks have been calculated and reported in Table S1; the derived values highlighted difference between GHDR 15–4 and Asbury graphite, with the last one more graphitic. Furthermore, the addition of Carbides additives, including the spark plasma synthetic pathway, brought to more ordered materials. The scanning electron microscopy (SEM) images, including energy dispersive spectroscopy (EDX) evidenced a uniform distribution of Si (green color) in the graphitic matrix (red color) for all samples. At the same time, also second phases of Mo (blue color) and Cr (blue color) were well dispersed, Figures 1d–g. All samples mechanical and electrical properties were also measured (Table S2). The results showed improved elastic modulus, flexural strength, and electrical conductivity in samples containing carbides, Asbury-MoC and Asbury-$Cr_3C_2$.[28–31] This is related to the fact that the presence of carbides chemically attached to graphite particles can provide bridges in all space directions (x,y,z)[28–32] positively impacting mechanical properties. Moreover, carbides are good electrical conductors, and their dispersion in the compound can increase electron transference, enhancing the electrical conductivity.[28–31,33]

### Electrochemical performance in Li-half cells

The electrochemical cycling tests were performed using the four compounds, with and without the addition of Si-nano-

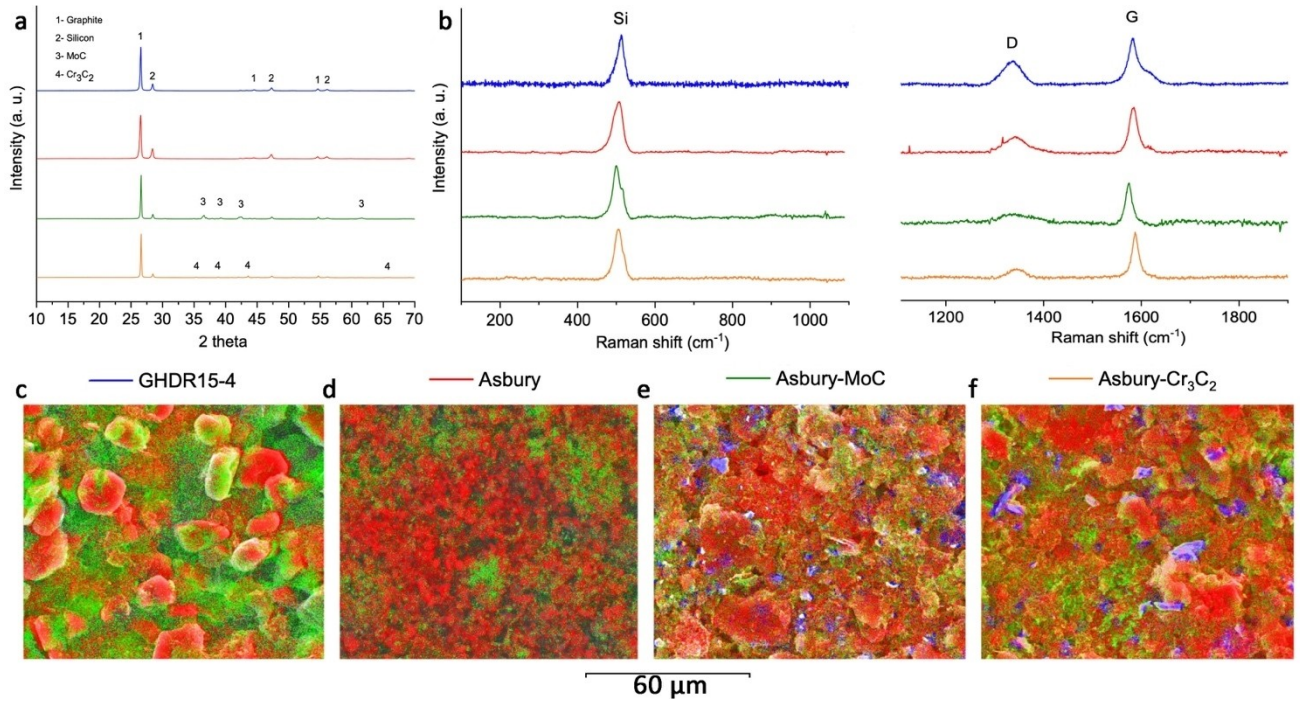


**Figure 1.** Pristine materials characterization: X-Ray diffraction patterns (**a**), Raman spectra (**b**) and SEM-EDX analysis for the GHDR15-4 (**c**, blue), Asbury (**d**, red), Asbury-MoC (**e**, green), Asbury-$Cr_3C_2$ (**f**, orange).

particles, as electrodes in Li-half cells; the cells were built using LP30 electrolyte (see the experimental section for composition). A first galvanostatic cycle is performed at C/10 rate (1 C = 3500 mA $g^{-1}$), to form a stable solid electrolyte interface at the surface of the particles and consequently stabilize the electrodes.[34–36] Following a current of C/3 is applied to evaluate the long-term performance of the compounds. The presence of Si improves the capacity for all materials, i.e., almost double, during the first cycle. Besides, the SEI formation occurs in the discharge process between 0.5–0.7 V, Figure 2;[37] in subsequent cycles, this slope change disappears (Figure S1). The first discharge involves in the range of potential below 0.2 V the lithiation process of $Li^+$ ion intercalation in the structure of the active material: $xLi^+ + 6\,C \rightarrow Li_xC_6$ $(0 < x \leq 1)$ and the Li-alloy formation: $yLi + Si \rightarrow Li_ySi$ $(1.71 < y \leq 4.4)$.[38, 39] In the following charge, the de-lithiation reaction of graphite, i.e., below 0.25 V, and de-alloying of Si, between 0.3 and 0.5 V, take place.[22,39–41] In this aspect, during the first cycle, the Li-cell using the pristine Asbury graphite and the Asbury-20%wt Si, Figure 2b, shows mostly the graphite intercalation and de-intercalation. The rest of the samples highlighted the graphite and silicon lithiation process.

After initial activation, during the first 100 cycles (Figure S2), all the electrodes (with and without Si-nanoparticles) showed similar trends, with initial capacity decay in the first ten cycles and following stabilization. Focusing more in detail on the evolution of this up to 100 cycles, Figure S2, it is observed how GHDR15.4 sample (a) reaches the stability at around cycle 40, and its capacity goes, approximately, from 125 to 250 mAh/g and Asbury sample (b) reaches the stability at around cycle 25 and its capacity increases of more >130% (from 90 mAh/g to 230 mAh/g). Finally, Asbury-MoC and Asbury-$Cr_3C_2$ samples (c and d) are stable above cycle 50, improving their capacity until ~200 mAh/g from less than 120 mAh/g. Therefore, the electrodes formed by active materials without carbides stabilize their capacity quickly, mainly because they are more sensitive to activation, and the gain in capacity is greater than those with carbides. Carbide presence causes the slower formation of stable SEI layer on particles, and stabilization up to running values,[39,42] apart from having lower theoretical specific capacity.[42,43] Asbury sample reaches stability sooner than the other, which can be the size and morphology of particles lower than the rest of the active materials and flakes.

Prolonged cycling performance were performed for over 400 cycles and reported in Figure 3. First, the cells were activated at C/20 current rate (Figure 3a), as the presence of carbides in the graphitic structure requires a longer time to form a stable SEI interface during the 1st cycle, with consequent activation of electrode particles upon cycling. Thus the formation of SEI is slowly, providing faster activation and stabilization of all materials, with improved delivered capacity: for GHDR15-4 above 300 mAh $g^{-1}$, Asbury around 275 mAh $g^{-1}$, Asbury-MoC to 250 mAh $g^{-1}$ and Asbury-$Cr_3C_2$ above 200 mAh $g^{-1}$. A major improvement is on prolonged cyclic performance, where electrodes with carbides in their structure showed very high stability. The different $Li_ySi$ phases formation

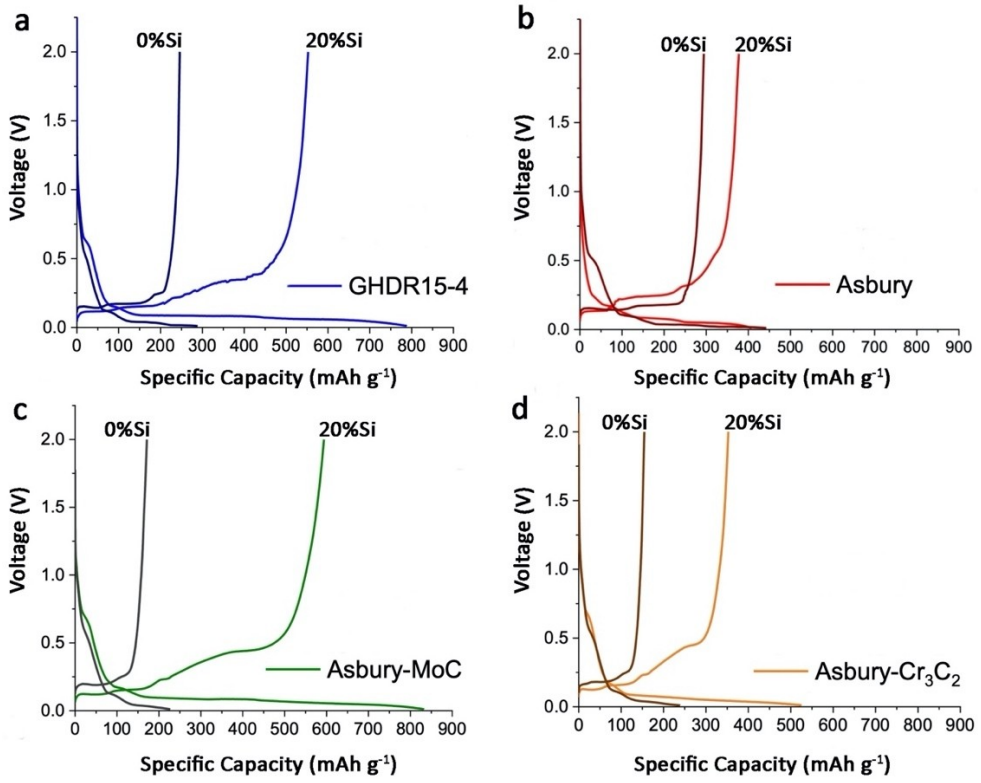


**Figure 2.** 1st cycle charge-discharge profile, C/10; cut off 0.01-2 V. Materials with and without 20% Si nanoparticles addition: GHDR15-4 **(a)**, Asbury **(b)**, Asbury-MoC **(c)**, Asbury-$Cr_3C_2$ **(d)**.

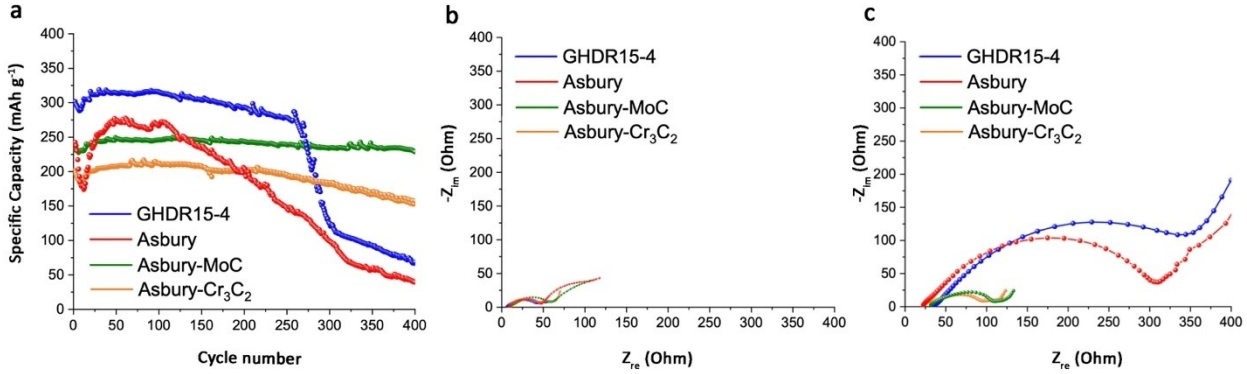


**Figure 3.** Cycle performance of the GHDR 15–4, Asbury, Asbury-MoC and Asbury-Cr3 C2 in Li-half cell using LP30 electrolyte **(a)**. Cut off 0.01-2 V; 1st cycle performed at C/20 and following C/3. Electrochemical impedance spectroscopy (EIS) of the Li-half cells using the four different electrodes at cycle 1st **(b)** and after 400th **(c)** cycles.

originates successive volume expansions in their internal structure during lithiation/delithiation processes.[44] This stress, generated by those sudden changes, leads to a fracture of the active material connections, producing a progressive disintegration of the electrode.[45] Consequently, the SEI layer is affected by Si cracking and pulverization, and part of the electrode surface is again exposed to the decomposition of the electrolyte through irreversible consumption of $Li^+$ ions to form a new SEI layer.[46–48] Since carbides were demonstrated to enhance the mechanical properties of the compound powder, see Table S1, the electrode and the associated SEI layer are more flexible, mitigating cracking due to huge volume changes, thus extending the cycle-life of the electrode.[22] Furthermore, adding $Cr_3C_2$ and MoC sintered with graphite can generate conductive channel networks that enormously improve the electrical conductivity (Table S1).[42] They provide stable morphology and conductive skeletons for the diffusion of $Li^+$ ions, increasing interfaces, and transfer of electrons.[22,49]

To investigate galvanostatic results, electrochemical impedance spectroscopy analysis (EIS) was carried out to evaluate the SEI interface resistance of electrodes at the 1st and after 400 cycles, Figure 3b and c.[50] The Li-ion half-cell system was modeled using a typical equivalent circuit,[50,51] represented in Figure S3. The overall resistance of electrodes containing carbides is maintained stable, Figures 3b and **c**, while the GHDR15-4 and Asbury electrodes highlighted a significant resistance increase.

All parameters resulting from the fitting analysis are reported in Table 1, where R1 corresponds to the Li-half cells bulk resistance, which includes the electrolyte, separator, and electrodes.[50] In all the cases after cycle 400, the R1 has the same range of values. R2 and Q1 are the resistance and capacitance of the SEI layer; R2 shows a significant increase in GHDR15-4 and Asbury cells after 400 cycles, indicating the SEI layer growing upon cycling. Q1 decreases for the graphite, specifying that the SEI layer is more compact and inorganic ($Li_2O$, LiF, $Li_2CO_3$, $SiO_2$). At the same time, Q1 slightly rises after 400 cycles in carbides, marking a porous and more organic SEI (lithium organic carbonates and carbon compounds). T1 is a time constant obtained by multiplying R1 and Q2; this indicates the time that $Li^+$ ions take to penetrate the SEI layer towards the active material surface. Lithium motion is shown slower in samples without carbides. Continuing with the analysis, R3 and Q2 represent the charge-transfer resistance and the related capacitance. R3 is stable in all samples and does not remarkably increase after 400 cycles. Carbides make electrochemical reactions easier, improving the charge transfer of electrons and $Li^+$ ions. Q2 refers to the electrochemically active area for the

**Table 1.** Electric parameters were obtained from the equivalent circuit fitted for the materials in the 1st and 400th cycles.

| Parameter | Cycle 1 (error ±5%) | | | | Cycle 400 (error ±5%) | | | |
|---|---|---|---|---|---|---|---|---|
| | GHDR15-4 | Asbury | Asbury-MoC | Asbury- $Cr_3C_2$ | GHDR15-4 | Asbury | Asbury- MoC | Asbury- $Cr_3C_2$ |
| R1 (elec.) [Ω] | 5.8 | 8.0 | 8.6 | 10.1 | 33.9 | 24.9 | 26.9 | 25.3 |
| R2 (SEI) [Ω] | 35.6 | 41.2 | 50.1 | 36.2 | 340.9 | 304.5 | 81.3 | 73.1 |
| Q1 [F] | $6.5\times10^{-5}$ | $6.7\times10^{-6}$ | $2.9\times10^{-5}$ | $2.1\times10^{-5}$ | $1.9\times10^{-5}$ | $3.4\times10^{-5}$ | $4.7*10^{-5}$ | $3.2\times10^{-5}$ |
| T1 = R2*Q1 [s] | $2.3\times10^{-3}$ | $2.8\times10^{-3}$ | $1.5\times10^{-3}$ | $1.1\times10^{-3}$ | $6.4\times10^{-3}$ | $10.4\times10^{-3}$ | $3.8*10^{-3}$ | $2.3\times10^{-3}$ |
| R3(Ch. Tr) [Ω] | 13.6 | 20.1 | 13.1 | 14.7 | 15.3 | 23.7 | 13.3 | 15.1 |
| Q2 [F] | $2.5\times10^{-3}$ | $2.8\times10^{-3}$ | $1.2\times10^{-3}$ | $2.3\times10^{-3}$ | $8\times10^{-4}$ | $1.6\times10^{-3}$ | $5\times10^{-3}$ | $3.1\times10^{-3}$ |
| T2 = R3*Q2 [s] | $3.4\times10^{-2}$ | $5.6\times10^{-2}$ | $1.6\times10^{-2}$ | $1.1\times10^{-2}$ | $1.2\times10^{-2}$ | $3.8\times10^{-2}$ | $6.6\times10^{-2}$ | $4.7\times10^{-2}$ |
| W1 [Ω] | $5.1\times10^{-2}$ | $1.3\times10^{-2}$ | $3.7\times10^{-2}$ | $4.9\times10^{-2}$ | $1.2\times10^{-4}$ | $3.1\times10^{-3}$ | $6.7\times10^{-2}$ | $5.3\times10^{-2}$ |
| W1 Change (%) | – | – | – | – | −99.8 | −76.2 | +81.1 | +8.2 |

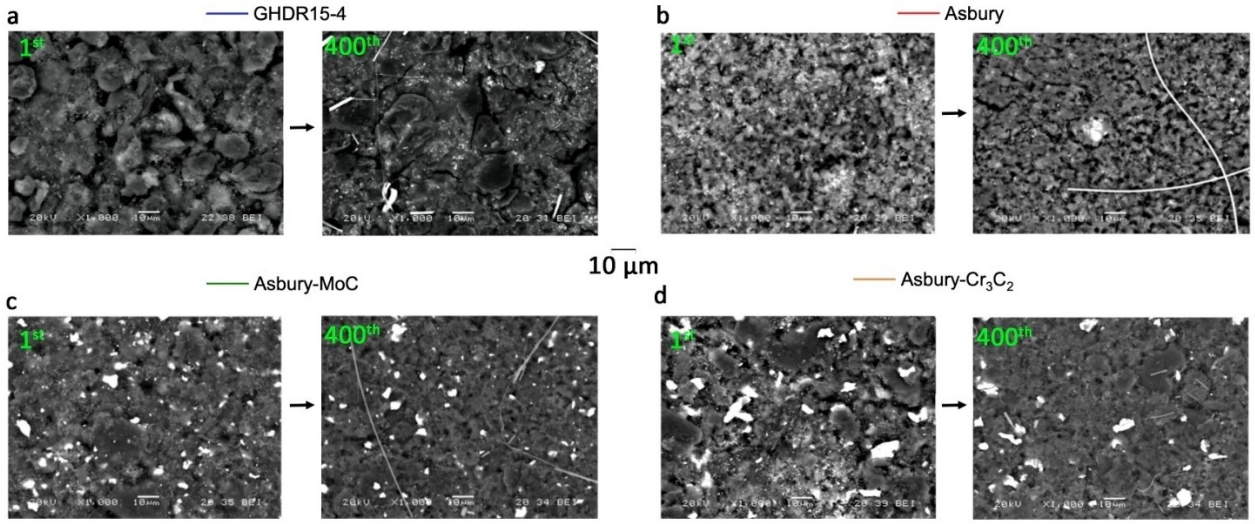


**Figure 4.** SEM images (BEI) of the materials after 1st and 400th cycles of discharge/charge. GHDR15-4 (a), Asbury (b), Asbury-MoC (c), Asbury-$Cr_3C_2$ (d).

redox reaction, which decreases in the samples composed only of graphite and silicon, while it remains stable when the material includes carbides. Finally, W1 is the Warburg impedance[50] and represents the $Li^+$ ions diffusion in the host material;[50] This is directly correlated with the diffusion coefficient. For the samples without carbides, W1 values strongly decrease, indicating a slower $Li^+$ ions motion inside the active material. The presence of carbides facilitates this transportation improving the diffusion. With this quantification, it can be affirmed that the presence of carbides helps the active material, specifically to the volume changes of silicon, providing structural integrity, more excellent electrical conductivity, and control of the side reactions to achieve an adequate capacity and spectacular stability for over 400 cycles.

To further support the Galvanostatic cycling performance and the SEI resistance improvements when including 5% carbides in the anodic powder, SEM images were collected on electrodes recovered after 1st and 400th cycles, Figure 4. SEM Images (BEI) give qualitative evidence of the cycling performance. In graphite without carbides (GHDR15-4: Figure 4a and Asbury: Figure 4b), it is plainly observed the degradation in the anode at cycle 400. There are big black zones evidencing the formation of a thick SEI layer, which limits the redox reactions with Li and cell operation. C, Si, O, and F content was also evaluated using SEM-EDX, see Table 1. For pristine commercial graphite, GHDR15-4 (Figure 4a) and Asbury graphite (Figure 4b) shows a strong degradation of the electrode surface between cycle 1st and 400th. The samples, including MoC, Figure 4c, and $Cr_3C_2$, Figure 4d, showed different surface images. In particular, the one including $Cr_3C_2$ shows a stable SEI layer but the presence of some holes in the surface, confirming the lower cycling stability of Figure 3, as SEI breaks down before than the one with molybdenum (IV) carbide (Figure 4c), which showed few signs of degradation. The ratio of C/Si, O/Si, and F/Si to confirm the aforementioned statements have been collected and reported in Table 2. In all cases, the percentages have increased as a consequence of electrolyte degradation on active material. However, materials with carbides experienced a lower rise.

The EDX analysis highlighted the composition of the SEI layer: silica ($SiO_2$), organic and inorganic lithium carbonates ($Li_2CO_3$), $Li_2O$, and LiF. The presence of oxygen, deriving from solvent decomposition, is an issue as it tends to oxidize metallic species, forming oxides, such as $SiO_2$, reducing the specific capacity, cycling stability, and reversibility of the electrochemical process. In this aspect, the presence of carbides acting as a scavenger for oxygen avoids the polarization of the surface and the formation of dangerous compounds such as silica. The white fibers appearing in the SEM images after 400 cycles are glass fibers derived from the separator used to build the Li-half cells.

**Table 2.** C/Si, O/Si, and F/Si ratio (considering wt. %) of the electrode materials recovered after 1st and 400th cycles.

| Material | C/Si | | O/Si | | F/Si | |
|---|---|---|---|---|---|---|
| | Cycle 1 | Cycle 400 | Cycle 1 | Cycle 400 | Cycle 1 | Cycle 400 |
| GHDR15-4 | 10.32 | 12.71 | 0.54 | 3.61 | 0.56 | 4.08 |
| Asbury | 13.64 | 20.57 | 0.76 | 5.49 | 0.44 | 4.86 |
| Asbury-MoC | 8.37 | 9.26 | 0.14 | 2.51 | 0.31 | 1.96 |
| Asbury-$Cr_3C_2$ | 9.10 | 10.86 | 0.21 | 2.53 | 0.38 | 2.99 |

## Conclusions

We showed that the presence of carbides based on Mo and Cr in a graphitic matrix including Si-nano particles produces a beneficial effect in terms of mechanical properties, alleviating Si-particle cracking due to huge volume changes during the lithiation processes. The cycling performance of these materials in Li-half cells showed improvements in delivered capacity and cycle life. Despite a Coulombic efficency slightly lower than pristine materials, the carbides added Silicon/Carbon electrodes showed an improved efficency and capacity retention for prolonged cycling, see Figure S4. This was also due to optimizing the activation steps, reducing the cycling current during the first discharge/charge to C/20 current rate, thus favoring the formation of a less compact and thick SEI layer, avoiding particles breaking upon $Li^+$ storage. The presence of carbide additives strongly stabilized the electrochemical performance over 400 cycles, with no sign of capacity fading. Deterioration mechanism was studied in pristine electrodes and compared with carbides added; SEM images revealed few signs of carbide based electrode deterioration, while EIS showed stable interface resistance and $Li^+$ diffusion in the active material matrix. Thus, in conclusion, using metal carbides in Si-based anodic materials opens the path to improve electrochemical performance and cycling stability.

## Experimental section

### Processing of graphite/silicon composites

Raw materials for the preparation of the graphite-silicon and graphite-metal carbides (MoC or $Cr_3C_2$)-silicon materials for the anodes consisted of:

- Battery-quality graphite (C-NERGY Actilion GHDR15-4 supplied by Imerys): purity 99.95%, with spheroidal morphology.
- Standard graphite (Asbury Carbons Company): purity 99%, with spheroidal-flake morphology.
- Molybdenum (H. C. Starck): purity 99.5%, with spheroidal morphology
- Chromium (Sigma Aldrich): purity $\geq$ 99%, with spheroidal morphology.
- Titanium (Abcr GMbh): purity 99.5%, with irregular morphology.
- Silicon (Ferroglobe): purity 99.9%, with spheroidal morphology and mean particle size ($d_{50}$) of 250 nm.

Spark plasma sintering has been used to prepare composites of graphite-MoC and graphite-$Cr_3C_2$. The graphite employed to fabricate the composites was non-specific for batteries, from Asbury Carbons Company. First, molybdenum (or chromium) and titanium powders were mixed in a roller mill with alumina balls for 24 h. Then, the mixture has been charged into the high-energy attrition mill (Union Process Inc. USA) with the graphite and 3 mm in diameter alumina balls, and it was mixed for 3 hours at a rate of 45 Hz. Mixtures have been prepared using isopropyl alcohol to facilitate the mixing and ensure a homogeneous material for later operations. Finally, the material was dried at 100 °C and sieved by 125 μm. Two types of compositions have been prepared based on the results in terms of electrical, mechanical, and thermal properties studied in other research works:[28–31]

Graphite-5.5 vol. % molybdenum-0.6 vol. % titanium.

Graphite-5.5 vol. % chromium-0.6 vol. % titanium.

Titanium has been used to stabilize α-$MoC_{1-x}$ carbide (cubic, unstable below 1960 °C).[28] In the case of chromium, the proportion of titanium has been maintained to avoid adding new compositional variables to the process.

Green compacts have been prepared by uniaxial pressing of the powder's mixtures at 20 MPa. Green specimens have been loaded into the graphite dies, and the heat treatment has been different depending on the composite to achieve the liquid phase sintering based on the carbon-molybdenum and carbon-chromium binary phase diagrams. This would lead a close contact between the graphite and the metal to promote the formation of the carbides:

Graphite-molybdenum system: dwell temperature of 2640 °C for 20 minutes under an applied pressure of 25 MPa.

Graphite-chromium system: dwell temperature of 2000 °C for 20 minutes under an applied pressure of 25 MPa.

The process has not been simple but a reactive sintering process, where the carbon has reacted with the metal to form the Carbide. The sintered discs, 170 mm in diameter and 20 mm in height with the already formed carbides were crushed and ground down to $<$75 μm. These powders have been used as raw materials for the anodes.

The mixtures of graphite-MoC, graphite-$Cr_3C_2$ and battery-quality graphite with 20 wt.% silicon nanoparticles have been prepared by low energy ball milling with 3 mm in diameter alumina balls and isopropyl alcohol at 100 rpm for 24 hours. Once dried and sieved by $<$180 μm, the powder was used to fabricate the anodes for electrochemical measurements.

### Electrochemical performance

- Electrode preparation: The active material based on Si, carbon black (conducting agent) and polyvinylidene dyfluoride (PVDF, polymer binder) were thoroughly mixed in an agate mortar with a weight proportion of 8:1:1. Then, by adding N-methyl pyrrolidone (NMP) in a relation 0.5 ml to 100 mg of active material, a black paste was prepared. Following, this was deposited on a copper foil using a doctor blade. The layer of 250 μm was dried in a heating plate for 24 h at 100 °C, with complete evaporation of NMP and moisture. Electrodes with 10 mm diameter and 3–4 mg loading were cut and dried in a tubular glass oven at 100 °C with a vacuum for 6 hrs.
- Coin cell manufacture: Li half-cells were assembled using electrodes inside a controlled atmosphere of Ar, where moisture and oxygen were below 0.1 ppm. A Whatman fiberglass separator with 18 mm diameter and Li counter electrode has been employed. As an electrolyte, 120 μl of 1 M $LiPF_6$ in EC:DMC (ethylene carbonate /dimethyl carbonate volume 1:1, named LP30) were added to the separator. Finally, the coin cell was closed using a 50 kg/cm$^2$ pressure.
- Electrochemical testing: galvanostatic cycling tests were carried out to evaluate the performance of the electrode materials (capacity and cycle-life). The current is established considering the reversible specific capacity of the silicon (3500 mAh/g) and its mass, assuming 1 C = 3500 mA/g. To get the whole capacity, it must be referred to as the total mass of the active material. For all the materials, the discharge/charge performance is divided into two steps: 1) activation cycle at C/10 or C/20, voltage cut off 0.01–2 V, and 2) the rest of the cycles at C/3 with a voltage cut off 0.01–2 V. All electrochemical measurements were made at room temperature (25 °C). To carry out tests only with the graphite (without silicon) as active material, the same current

density (J [mA/g]) is imposed with the purpose of calculating the current and making a comparison with silicon.

EIS (electrochemical impedance spectroscopy) studied the interface resistances and electrode processes by applying a 10 mV AC amplitude signal to Li symmetrical cell in a 500 kHz to 100 mHz frequency range. The interface and charge transfer resistance were evaluated by the nonlinear least squares (NLLS) fit of the semicircles observed in the Nyquist plots. The Nyquist plots related to the Li cells stability show the semicircles associated with film formation and charge-transfer processes located at high and low-frequency regions, respectively. The equivalent circuit used for the NLLS fit was R(RQ)(RQ)W, where R represents the resistance, Q is the constant phase element (CPE), and W is the Warburg resistance.

To analyze postmortem electrodes, they must be processed inside the glovebox when the cells are disassembled. Afterward, the electrodes are cleaned with dimethyl carbonate (DMC, Merk) and tetrahydrofuran (THF, Merk) to remove soluble contaminants and the salt remains. Finally, they are dried for half an hour under vacuum conditions and saved inside vials in the glove box.

### Characterization techniques

X-ray diffraction technique has been employed for the identification of the mineralogical phases. It consisted of a Bruker Advanced Powder X-ray diffractometer model D8 with Cu-kα radiation ($\lambda = 0.15406$ nm). Copper anticathode water cooled with an intensity of 40 mA and a voltage of 40 kV, a swept between 10–70° with a step of 0.02° and a step time of 0.2 s were the working conditions. Peak fitting of the crystalline phases was performed by diffraction pattern files provided by JCPDS (International Centre for Diffraction Data), using Xpowder Software.

Raman analysis was performed using a Dilor LabRam micro-Raman Spectrometer utilizing a HeNe 632.8 nm, 4.7 mW laser; 1800 grooves mm$^{-1}$ grating; and an X50 objective.

MEB JEOL-6610LV with microanalysis INCA Energy-350 has been employed for the microstructural characterization of the pristine material in cycles 1 and 400. The mapping of elements was provided by Energy-dispersive X-ray spectroscopy (EDX). The back-scattered electron imaging (BEI) mode has been employed in the Field Emission Scanning Electron Microscope (SEM) on a Quanta FEG 650.

The flexural strength was determined on specimens of 3 mm x 4 mm×20 mm. The equipment was a Shimadzu-Serie AGS-IX test machine. The flexural strength ($\sigma_f$, in Mpa) of the samples measured using the three-point bending test has been evaluated using equation (2).

$$\sigma_f = \frac{3 \cdot P \cdot L}{2 \cdot w \cdot b^2} \quad (2)$$

Where $P$ is the failure load in N, $L$ is the distance between supports (span, 12.5 mm) in mm, $w$ is the width of the sample in mm, and $b$ is the thickness of the sample in mm.

The Young's modulus was measured using a Grindsonic (MK, Belgium) equipment on 3 mm×4 mm×20 mm samples.

The electrical conductivity was measured by a four-point probe test in the in-plane direction using the equipment PSM1735 – NumetriQ – Newtons 4$^{th}$.

## Acknowledgements

Juan Piñuela Noval acknowledges the Programa "Severo Ochoa" of Grants for Research and Teaching of the Principality of Asturias for the funds received for the elaboration of the Ph. D. Thesis (Ref.: BP20 041). Juan Piñuela Noval also thanks the grant "Ayuda de Estancias Breves en otros Centros de Investigación" within the Programa "Severo Ochoa" for the training in research and teaching in 2022 (Ref.: EB22-11). Daniel Fernández-González acknowledges the grant (Juan de la Cierva-Formación program) FJC2019-041139-I funded by MCIN/AEI/10.13039/501100011033 (Ministerio de Ciencia e Innovación, Agencia Estatal de Investigación). This research was supported by the project Investigación industrial de materiales estratégicos para baterías de ión-litio de alta densidad energética y coste optimizado en electromovilidad sostenible LiOn-HD, promoted by Iniciativas Estratégicas Sectoriales de Innovación Empresarial (Programa "Misiones CDTI"), en el marco del Programa Estatal de Liderazgo Empresarial en 1+D+I, del Plan Estatal de Investigación Científica y Técnica y de Innovación 2017–2020. Science and Innovation Ministery of Spain. Authors are grateful to Ainhoa Macías San Miguel from Nanomaterials and Nanotechnology Research Center (CINN) for providing technical assistance.

## Conflict of Interests

The authors declare no conflict of interest.

## Data Availability Statement

The data that support the findings of this study are available from the corresponding author upon reasonable request.

**Keywords:** Li-ion batteries · silicon · molybdenum carbide · chromium carbide · anode · graphite

[1] H. J. Kim, T. N. V. Krishna, K. Zeb, V. Rajangam, C. V. V. M. Gopi, S. Sambasivam, K. V. G. Raghavendra, I. M. Obaidat, *Electronics.* **2020**, *9*, 1161.
[2] H. Gong, J. Sun, *Encyclopedia of Nanomaterials.* **2023**, *2*, 533–549.
[3] T. Kim, W. Song, D.-Y. Son, L. K. Ono, Y. Qi, *J. Mater. Chem. A* **2019**, *7*, 2942.
[4] C. Chaves, E. Pereira, P. Ferreira, A. G. Dias, *The Extractive Industries and Society.* **2021**, *8*, 100928.
[5] H. Vikström, S. Davidson, M. Höök, *Appl. Energy* **2013**, *110*, 252–266.
[6] S. Chae, S.-H. Choi, N. Kim, J. Sung, J. Cho, *Angew. Chem. Int. Ed.* **2019**, *59*, 110–135.
[7] T. Yoon, C. C. Nguyen, D. M. Seo, B. L. Lucht, *J. Electrochem. Soc.* **2015**, *162*, A2325-A2330.
[8] D. Aurbach, *J. Power Sources* **2020**, *89*, 206–218.
[9] C. K. Chan, R. Ruffo, S. S. Hong, Y. Cui, *J. Power Sources* **2009**, *189*, 1132–1140.
[10] P. Verma, P. Maire, P. Novak, *Electrochim. Acta* **2010**, *55*, 6332–6341.
[11] H. Wu, Y. Cui, *Nano Today* **2012**, *7*, 414–429.
[12] J.-Y. Li, Q. Xu, G. Li, Y.-X. Yin, L.-J. Wan, Y.-G. Guo, *Mater. Chem. Front.* **2017**, *1*, 1691–1708.
[13] N. P. Wagner, A. Tron, J. R. Tolchard, G. Noia, M. P. Bellmann, *J. Power Sources* **2019**, *414*, 486.
[14] P. Li, H. Kim, S.-T. Myung, Y.-K. Sun, *Energy Storage Mater.* **2021**, *35*, 550.

[15] E. Moyassari, T. Roth, S. Kücher, C.-C. Chang, S.-C. Hou, F. B. Spingler, A. Jossen, *J. Electrochem. Soc.* **2022** *169*, 010504.
[16] M. Otero, C. Heim, E. P. M. Leiva, N. Wagner, A. Friedrich, *Sci. Rep.* **2018**, *8*, 15851.
[17] N. Hamzelui, G. G. Eshetu, E. Figgemeier, *J. Energy Storage* **2021**, *35*, 102098.
[18] Z. Li, Y. Yang, Z. Wan, X. Zeng, L. Yan, S. Wu, M. Ling, C. Liang, K. N. Hui, Z. Lin, *Adv. Energy Mater.* **2022**, *12*, 2201197.
[19] G. G. Eshetu, E. Figgemeier, *ChemSusChem* **2019**, *12*, 2488–2828.
[20] Y. Zhou, H. Sun, M. H. Uddin, M. K. S. Barr, D. Wisser, P. Robmann, J. D. Esper, S. Tymek, D. Döhler, W. Peukert, M. Hartmann, J. Bachmann, *Electrochim. Acta* **2021**, *388*, 138522.
[21] W. Sun, R. Hu, H. Liu, H. Zhang, J. Liu, L. Yang, H. Wang, M. Zhu, *Electrochim. Acta* **2016**, *191*, 462.
[22] Y. Liu, W. Sun, X. Lan, R. Hu, J. Cui, J. Liu, J. Liu, Y. Zhang, M. Zhu, *ACS Appl. Mater. Interfaces* **2019**, *11*, 3872.
[23] W. Pan, X. Cai, C. Yang, L. Zhou, *J. Electron. Mater.* **2021**, *50*, 2584–2593.
[24] K. Xu, X. Li, X. Liu, Y. Yu, X. Zhang, W. Lei, Z. Xie, S. Zhang, Q. Jia, H. Zhang, *Sustain. Mater. Technol.* **2023**, *36*, e00583.
[25] S. Komaba, N. Yabuuchi, T. Ozeki, Z.-J. Han, K. Shimomura, H. Yui, Y. Katayama, T. Miura, *J. Phys. Chem. C* **2012**, *116*, 1380.
[26] J. Nanda, M. K. Datta, J. T. Remillard, A. O'Neill, P. N. Kumta, *Electrochem. Commun.* **2009**, *11*, 235.
[27] M. A. Cabañero, M. Hagen, E. Quiroga-González, *Electrochim. Acta* **2021**, *374*, 137487.
[28] M. Suárez, D. Fernández-González, C. F. Gutiérrez-González, L. A. Díaz, A. Borrell, J. S. Moya, R. Torrecillas, A. Fernández, *J. Eur. Ceram. Soc.* **2022**, *42*, 2048.
[29] M. Suárez, D. Fernández-González, L. A. Díaz, J. Piñuela-Noval, A. Borrell, J. S. Moya, R. Torrecillas, A. Fernández, *Boletín de la Sociedad Española de Cerámica y Vidrio.* **2023**, in press. https://doi.org/10.1016/j.bsecv.2023.02.005.
[30] M. Suárez, D. Fernández-González, L. A. Díaz, A. Borrell, J. S. Moya, A. Fernández, *Ceram. Int.* **2021**, *47*, 30993.
[31] J. Piñuela-Noval, D. Fernández-González, M. Suárez, L. A. Díaz, L. F. Verdeja, A. Fernández, *J. Am. Ceram. Soc.* **2023**, in press. https://doi.org/10.1111/jace.19145.
[32] J. Guardia-Valenzuela, A. Bertarelli, F. Carra, N. Mariani, S. Bizzaro, R. Arenal, *Carbon* **2018**, *135*, 72.
[33] N. Mariani, Development of Novel, Advanced Molybdenum-based Composites for High Energy Physics Applications, **2014**, Ph. D Thesis (Supervisor: A. Bertarelli), Politecnico di Milano, Milan, Italy.
[34] Y. Liu, W. Sun, X. Lan, R. Hu, J. Cui, J. Liu, J. Liu, Y. Zhang, M. Zhu, *ACS Appl. Mater. Interfaces* **2019**, *11*, 38727.
[35] W. Sun, R. Hu, H. Zhang, Y. Wang, L. Yang, J. Liu, M. Zhu, *Electrochim. Acta* **2016**, *187*, 1.
[36] Y. Zhou, H. Guo, Y. Yang, Z. Wang, X. Li, R. Zhou, W. Peng, *Mater. Lett.* **2016**, *168*, 138.
[37] C. Bongiorno, G. Mannino, U. D'Alessio, F. Monforte, G. G. Condorelli, C. Spinella, A. La Magna, S. Brutti, *Energy Technol.* **2021**, *10*, 2100791.
[38] B. A. Boukamp, G. C. Lesh, R. A. Huggins, *J. Electrochem. Soc.* **1981**, *128*, 725.
[39] K. Xu, X. Li, X. Liu, Y. Yu, X. Zhang, W. Lei, Z. Xie, S. Zhang, Q. Jia, H. Zhang, *Sustain. Mater. Technol.* **2023**, *36*, e00583.
[40] B. Fuchsbichler, C. Stangl, H. Kren, F. Uhlig, S. Koller, *J. Power Sources* **2011**, *196*, 2889.
[41] Q. Xu, Q. Wang, D. Chen, Y. Zhong, Z. Wu, Y. Song, G. Wang, Y. Liu, B. Zhong, X. Guo, *Green Chem.* **2021**, *23*, 4531.
[42] W. Pan, X. Cai, C. Yang, L. Zhou, *J. Electron. Mater.* **2021**, *50*, 2584.
[43] Y. Liu, W. Sun, X. Lan, R. Hu, J. Cui, J. Liu, J. Liu, Y. Zhang, M. Zhu, *ACS Appl. Mater. Interfaces* **2019**, *11*, 38727.
[44] N. Cuesta Pedrayes, Materiales anódicos alternativos para el desarrollo de baterías de ión-litio sostenibles, **2016**, Ph.D. Thesis (supervisors: I. Cameán Martínez and A. E. Ramos Alonso) Instituto Nacional del Carbón-Consejo Superior de Investigaciones Científicas (INCAR-CSIC)-Universidad de Oviedo, Oviedo/Uviéu, Asturias, Spain.
[45] M. N. Obrovac, L. Christensen, *Electrochem. Solid-State Lett.* **2004**, *7*, A93.
[46] M. T. McDowell, S. W. Lee, W. D. Nix, Y. Cui, *Adv. Mater.* **2013**, *25*, 4966–4985.
[47] N. Liu, H. Wu, M. T. McDowell, Y. Yao, C. Wang, Y. Cui, *Nano Lett.* **2012**, *12*, 3315.
[48] B. Scrosati, J. Garche, *J. Power Sources* **2010**, *195*, 2419.
[49] W. Sun, R. Hu, H. Liu, H. Zhang, J. Liu, L. Yang, H. Wang, M. Zhu, *Electrochim. Acta* **2016**, *191*, 462.
[50] W. Choi, H.-C. Shin, J. M. Kim, J.-Y. Choi, W.-S. Yoon, *J. Electrochem. Sci. Technol.* **2020**, *11*, 1–13.
[51] N. S. Zhai, M. W. Li, W. L. Wang, D. L. Zhang, D. G. Xu, *J. Phys. Conf. Ser.* **2006**, *48*, 1157.

Manuscript received: July 18, 2023
Revised manuscript received: September 26, 2023
Version of record online: October 12, 2023